communications physics

A Nature Portfolio journal

Article

https://doi.org/10.1038/s42005-025-02012-5

Efficient measurement and representation of magnetic fields in tomographic imaging using ellipsoidal harmonics

Konrad Scheffler [1,2] ✉, Lara Meyn [2], Fynn Foerger [1,2], Marija Boberg [1,2], Martin Möddel [1,2] & Tobias Knopp [1,2,3]

Given the pivotal role of magnetic fields in modern medicine, there is an increasing necessity for a precise characterization of their strength and orientation at high spatial and temporal resolution. As source-free magnetic fields present in tomographic imaging can be described by harmonic polynomials, they can be efficiently represented using spherical harmonic expansions, which allows for measurement at a small set of points on a sphere surrounding the field of view. However, the majority of closed-bore systems possess a cylindrical field of view, making a sphere an inadequate choice for coverage. Ellipsoids represent a superior geometrical choice, and the theory of ellipsoidal harmonic expansions can be applied to magnetic fields in an analogous manner. Despite the mathematical principles underpinning ellipsoidal harmonics being well-established, their utilization in practical applications remains relatively limited. In this study, we present an effective and flexible approach to measuring and representing magnetic fields present in tomographic imaging, which draws upon the theory of ellipsoidal harmonic expansions.

Magnetic fields are the basis for many applications in future medicine and play an important role in both diagnostics and therapy. For example, they can be used to drive and control magnetic micro- and nanorobots for various potential biomedical applications. Such robots have great potential in many areas of medicine as they can perform medical procedures even in remote and sensitive parts of the human body. This includes targeted delivery and release of drugs and therapeutics, cell manipulation, and minimally invasive surgery such as stenting[1–8]. In addition, magnetic fields are used to visualize, navigate, and heat magnetic nanoparticles, allowing the focal treatment of tumors with hyperthermia[9,10]. Finally, magnetic fields are at the heart of the tomographic imaging techniques magnetic resonance imaging (MRI) and magnetic particle imaging (MPI)[11] and magnetorelaxometry[12]. Here, knowledge of the exact values of the magnetic fields in the field of view (FOV) is of great importance for signal encoding[13,14].

In particular, the complex setup of coils or permanent magnets often leads to non-ideal magnetic fields and the benefits of accurate knowledge of the magnetic fields are manifold. Firstly, it is essential for hardware development, particularly in designing and arranging magnetic field generators to achieve ideal fields in the scanner's FOV. In the context of low-field MRI systems, which are increasingly important in the context of low-cost and point-of-care systems, high B_0-field homogeneity is a crucial factor in ensuring high-quality images[15–17]. Similarly, the non-linearity of gradient fields plays a major role in image quality[15,18–20], so knowledge of magnetic fields is important and enables verification and quality control of imaging systems in both science and industry. Furthermore, it can be used for a precise sequence design in MRI. Moving on to image reconstruction, knowledge of the magnetic fields is very important to account for field inhomogeneity and reduce off-resonance artifacts[21–26]. Moreover, field values can be used to enhance various reconstruction methods and mitigate the reconstruction error[27,28].

Measurements of a magnetic field in tomographic imaging can be performed using a magnetic field sensor, such as a Hall sensor or an inductive sensor[29]. To cover a three-dimensional FOV, the sensor is moved voxel by voxel through the FOV along a dense grid. An increase in spatial resolution directly correlates with an expansion in the number of

[1]Section for Biomedical Imaging, University Medical Center Hamburg-Eppendorf, Hamburg, Germany. [2]Institute for Biomedical Imaging, Hamburg University of Technology, Hamburg, Germany. [3]Fraunhofer Research Institution for Individualized and Cell-based Medical Engineering IMTE, Lübeck, Germany.
✉e-mail: konrad.scheffler@tuhh.de

measurement points, making this naive measurement procedure both time-consuming and labour-intensive. For illustration, a bisection of the distances results in eight times the number of measurement points. A more sophisticated alternative to the measurement on a dense grid is to employ spherical harmonics, given that source-free magnetic fields satisfy Laplace's equation and can thus be expanded into a series of spherical harmonic functions[30]. In scenarios where magnetic fields can be adequately represented by low-degree polynomials, it becomes feasible to truncate the series at an early stage. This approach enables the implementation of efficient measurement methods that require only a limited number of field evaluation points defined by a spherical t-design. A t-design is a sampling distribution that facilitates the exact integration of polynomials up to degree t[31,32]. The magnetic field values can then be derived at any position within the sphere, i.e., sampled at any resolution. Spherical harmonic expansions also allow for a higher temporal resolution of magnetic field measurements. However, one limitation is that the size of the sphere is fixed in advance. Tomographic imaging systems with a closed bore often have a cylindrical shape. The bores are meant to fit a rodent, a human head or extremities, or even the whole human body. To cover a cylindrical FOV (shown by the green line in Fig. 1), several spheres need to be shifted along the bore axis (indicated by the red dashed lines). Each sphere must be measured independently and the results combined. This process is tedious, reduces the temporal resolution of the measurements, and can leave parts of the FOV uncovered.

If we consider an ellipsoid instead, we gain two more degrees of freedom to adopt its shape. Thus, a cylindrical FOV can be covered much better (as shown by the blue dotted line in Fig. 1). The theory of ellipsoidal harmonic functions as a basis of harmonic polynomials is well known. Although the series expansion is comparable to that of spherical harmonics, the underlying derivations for ellipsoidal coordinates are more complex. While ellipsoidal harmonic expansions have been studied in several scientific fields, such as chemical physics[33] and fluid dynamics[34], translations to practical applications are rare. In astrophysics they allow a more efficient calculation of the gravitational potential of celestial bodies[35]. Potential applications are also conceivable in other scientific fields that rely on solving equation systems of similar structure, for example plasma science[36]. For magnetic fields, and particularly in tomographic imaging, ellipsoidal harmonics have been studied to improve MRI shimming on an ellipsoidal region of interest[37–40]. Moreover, ellipsoidal coordinates can be used to improve methods in many areas of medical applications, e.g., reconstruction of ellipsoidal areas with a minimal number of radiographs in computed tomography[41], brain activity in ellipsoidal geometry[42], and electroencephalography on ellipsoidal surfaces[43]. In the context of application, effective and accurate methods for calculating the arising surface integrals are important. In this context, a variable splitting combined with Gauss quadratures has been presented[38]. Recently, a semi-analytical approach for the computation of ellipsoidal harmonics has been presented[44]. However, it is noted that for higher degree polynomials, a numerical approach is slower but more stable and accurate. It is to the best of the authors' knowledge that there is no existing literature on the use of spherical t-designs shifted to an ellipsoidal surface for the efficient computation of ellipsoidal harmonic expansions. Furthermore, there is a lack of publicly available software packages on the topic of ellipsoidal harmonics. Open-source implementations in MATLAB and Python have been presented in ref. 45 using a simple midpoint quadrature to solve the surface integrals that arise in this context. However, this method is known to be slow to converge.

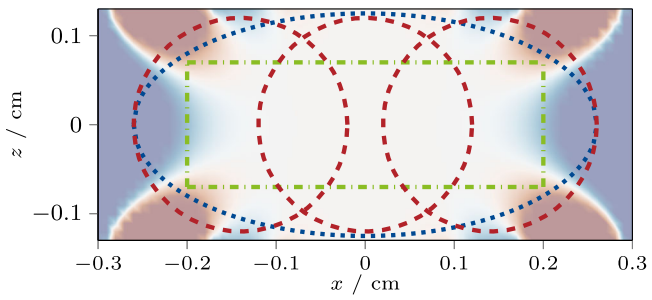

Fig. 1 | Field of view coverage in an homogeneous field with shifted spheres and ellipsoid. Shown is the coverage of an cylindrical field of view (displayed as a green line) when using several shifted spheres (displayed as red dashed lines) and an ellipsoid (displayed as a blue dotted line) in the central x, z-plane of the permanent magnet B_0-field presented by O'Reilly et al.[51]. The B_0-field is indicated in the background.

The geometric shape of prolate and oblate spheroids is an intermediate between spheres and ellipsoids. Thus, they are less flexible in covering a given FOV than ellipsoids, but still an improvement over spheres. Spheroidal harmonics could offer an advantage over ellipsoidal harmonics in some settings because their derivation is less complex[46–49]. However, this work focuses on the more flexible ellipsoidal case.

The principal objective of this study is to demonstrate that ellipsoidal harmonics can be employed to effectively measure and represent magnetic fields in tomographic imaging. The following section outlines the structure of the paper. A brief introduction to ellipsoidal harmonics, along with a review of the necessary ingredients for their implementation in practice is given in the "Methods" section. For readers interested in further details, additional information is provided in the last three subsections of section "Methods", while the cited literature contains derivations and more detailed explanations of the mathematics. The application of ellipsoidal harmonic expansions to simulated magnetic fields present in MRI is demonstrated. A comparison with spherical harmonic expansions is provided to illustrate the potential of ellipsoidal harmonics in tomographic imaging. The software tool, written in Julia, is published as an open source package.

At the 2024 International Workshop on MPI, the authors presented preliminary results on utilizing ellipsoidal harmonic expansions to represent magnetic fields in magnetic particle imaging[50].

Results

The main objective of this work is showcasing that magnetic fields in tomographic imaging can be represented efficiently by using ellipsoidal harmonic expansions. To illustrate this, we have performed simulation studies on magnetic fields present in MRI. The implementation of the ellipsoidal harmonic expansion was written in Julia and is published under the MIT License at https://github.com/IBIResearch/EllipsoidalHarmonicExpansions. The polynomial calculations and the root finding are based on the package Polynomials.jl (https://github.com/JuliaMath/Polynomials.jl). For spherical harmonic expansions the Julia package SphericalHarmonicExpansions.jl (https://github.com/hofmannmartin/SphericalHarmonicExpansions.jl) was used.

Experimental design: homogeneous field

Constant and ideally homogeneous B_0 fields are essential in MRI, as they polarize spins and generate magnetization. The development of B_0 fields with low energy consumption and small system size is an important topic of current research in the emerging field of low-field MRI. Arrays of permanent magnets arranged in a discretized version of a Halbach ring can be used to produce B_0 fields, where a high length-to-diameter ratio is important for high homogeneity. The higher this ratio, the more suitable ellipsoidal harmonics are for efficient field measurement compared to spherical harmonics. Such a Halbach configuration for a potential low-field and low-cost MRI with length-to-diameter ratio of 2:1 was presented by O'Reilly et al.[51]. The setup consists of 23 double rings with 27 cm bore diameter. In total 2948 cuboid N48 neodynium magnets are used to generate a homogeneous 50 mT field transversal to the bore (in positive z-direction). A simulation of the setup was conducted on a three-dimensional grid comprising $61 \times 27 \times 27$ grid points and a point distance of 1 cm. This was achieved by superpositioning the magnetic fields calculated in accordance with the Biot-Savart law based on the surface currents of each individual magnet. The simulated field was interpolated to the data points of the t-designs by using cubic splines.

The reference ellipsoid was chosen with semi-axes $\boldsymbol{a} = (0.26, 0.125, 0.1249)$ m around the coordinate origin in the center of the Halbach configuration to comprise a cylindrical FOV (Ω_{FOV}) with 0.2 m height and 0.07 m radius as shown in Fig. 1. To calculate the inner ellipsoidal harmonics, a 14-design comprising 114 data points on the reference ellipsoid was employed. Although the simulated magnetic field has a large homogeneous area, it is reasonable to assume that a t-design of this scale is necessary to accurately represent the inhomogeneities in the outer region. To validate this assumption, an ellipsoidal harmonic expansion was performed on the same reference ellipsoid using an 8-design containing only 44 data points. In addition, we also considered the conjunction of three spheres with radius 0.12 m, shifted along the x-axis to cover the FOV. Here, three separate 14-designs with 114 data points per sphere (i.e., a total of 342 data points) were used to compute the spherical harmonic expansion. Thus, in this case, the ellipsoidal representation using a single 14-design is three times more efficient than the spherical representation. Furthermore, we consider the same spheres with three separate 7-designs, each comprising 38 data points. This ensures that the total number of 114 data points is comparable to the number of data points in the ellipsoidal 14-design. The cylindrical FOV, the reference ellipsoid and the spheres are shown in Fig. 1.

For a quantitative evaluation we set the simulated B_0 field as ground truth and consider difference maps of the locally normalized root mean squared deviation to the fields calculated by both harmonic expansions:

$$\xi^{B_0}_{\mathrm{EHE}} := \frac{\|\boldsymbol{B}_{\mathrm{EHE}} - \boldsymbol{B}\|_2}{\|\boldsymbol{B}\|_2}, \qquad \xi^{B_0}_{\mathrm{SHE}} := \frac{\|\boldsymbol{B}_{\mathrm{SHE}} - \boldsymbol{B}\|_2}{\|\boldsymbol{B}\|_2}. \tag{1}$$

Experimental design: gradient field

Gradient fields play an important role in spatial encoding in tomographic imaging. Exemplarily we consider the MRI B_0 field produced by the permanent Halbach configuration again. Appropriate coil setups for optimized linear gradients in each spatial direction have been presented by De Vos et al.[52]. Using their gradient design tool (https://github.com/LUMC-LowFieldMRI/GradientDesignTool/tree/master) and the FEM software COMSOL Multiphysics (v.6.0. www.comsol.com. COMSOL AB, Stockholm, Sweden) a linear gradient was simulated along the bore, with the field oriented transversally in the direction of B_0 on the same grid as that used for the B_0 field. As previously, the simulated field was interpolated to the data points of the t-designs by using cubic splines.

Because of the highly non-linear parts of the field in the vicinity of the coils, the reference ellipsoid was chosen with semi-axes $\boldsymbol{a} = (0.25, 0.1, 0.099)$ m around the coordinate origin in the center of the Halbach configuration to comprise a cylindrical FOV with 0.18 m height and 0.06 m radius as shown in Fig. 2. For comparison we consider again the conjunction of three spheres with radius 0.1 m, shifted along the x-axis. The t-designs were chosen analogously to the B_0 case: a single 14-design with 114 data points on the ellipsoid and three separate 14-designs with 114 data points on each sphere. Studies with smaller t-designs on the gradient field show a similar effect as shown for the B_0 field. Therefore, we do not show it again to avoid redundancy.

For an error analysis, the simulated gradient field is considered as ground truth and difference maps of the globally normalized root mean squared deviation to the fields calculated by both harmonic expansions:

$$\xi^{\mathrm{grad}}_{\mathrm{EHE}} := \frac{\|\boldsymbol{B}_{\mathrm{EHE}} - \boldsymbol{B}\|_2}{\max_{\Omega_{\mathrm{FOV}}} \|\boldsymbol{B}\|_2}, \qquad \xi^{\mathrm{grad}}_{\mathrm{SHE}} := \frac{\|\boldsymbol{B}_{\mathrm{SHE}} - \boldsymbol{B}\|_2}{\max_{\Omega_{\mathrm{FOV}}} \|\boldsymbol{B}\|_2}. \tag{2}$$

It should be noted that a local normalization would result in a singularity due to the zero crossing of the gradient field. Therefore, a global error normalization using the maximum value inside the FOV was selected as an alternative.

Experimental results: homogeneous field

Exemplary results of the B_0 field in the x, z-plane are shown in Fig. 3. In the second column, the calculated fields are given next to the ground truth. When using the 14-design, no visual differences are detectable inside the volume of the reference ellipsoid. Towards the edges and outside of these regions, slight differences can be seen. This becomes clearer when looking at the difference plots in the right column. The relative error is smaller than 1% in most of the FOV, becomes slightly larger towards the edges of the ellipsoid (up to 5%), and increases rapidly outside the FOV. A consideration of the difference plot of the ellipsoidal harmonic expansion with the smaller 8-design reveals that the error increases more strongly inside the reference ellipsoid, yet remains below 10%. A similar behavior is observed in the conjunction of the three spheres. With 14-designs, the error is smaller than 1% inside the spheres. However, when using 7-designs, the error is visibly larger in the outer spheres, where the field tends to become less homogeneous. In this case, the result is clearly worse than for the ellipsoidal harmonic expansion with one 14-design, despite using the same total number of data points.

Firstly we consider the quantitative results for the ellipsoidal harmonic expansion on the B_0-field when using a smaller 8-design with only 44 data points. This method yielded a mean error of $\mathrm{mean}_{\Omega_{\mathrm{FOV}}}(\xi^{B_0}_{\mathrm{EHE}_8}) = 1.22\%$ and a maximum error of $\max_{\Omega_{\mathrm{FOV}}}(\xi^{B_0}_{\mathrm{EHE}_8}) = 5.78\%$ inside the cylindrical FOV. The error exhibited an increase outside the FOV, approaching the edge of the reference ellipsoid, as can be observed in Fig. 3. In the context of the ellipsoidal 14-design with 114 data points, a mean error of $\mathrm{mean}_{\Omega_{\mathrm{FOV}}}(\xi^{B_0}_{\mathrm{EHE}_{14}}) = 0.32\%$ and a maximum error of $\max_{\Omega_{\mathrm{FOV}}}(\xi^{B_0}_{\mathrm{EHE}_{14}}) = 3.64\%$ were attained within the FOV. This signifies a substantial enhancement over the 8-design. The error is negligible in the center of the reference ellipsoid, increasing towards the border.

For validation of the presented methods we also consider the error for the spherical harmonic expansions. Considering the field resulting from the concatenation of three spherical harmonic expansions with 7-designs and thus the same number of 114 total data points, a mean error of $\mathrm{mean}_{\Omega_{\mathrm{FOV}}}(\xi^{B_0}_{\mathrm{SHE}_7}) = 0.55\%$ and a maximum error of $\max_{\Omega_{\mathrm{FOV}}}(\xi^{B_0}_{\mathrm{SHE}_7}) = 4.12\%$ was achieved inside the FOV. A mean error of $\mathrm{mean}_{\Omega_{\mathrm{FOV}}}(\xi^{B_0}_{\mathrm{SHE}_{14}}) = 0.09\%$ and a maximum error of $\max_{\Omega_{\mathrm{FOV}}}(\xi^{B_0}_{\mathrm{SHE}_{14}}) = 0.54\%$ inside the FOV was achieved with threefold data points using the concatenation of results on three shifted spherical harmonic expansions with 14-designs.

Experimental results: gradient field

Qualitative results of the gradient field are plotted in the x, y-plane (transversal to the B_0-direction) in Fig. 4. The field points in B_0-direction (positive z), thus no field arrows are displayed. Inside the regions of convergence (respectively the reference ellipsoid and the conjunction of the three spheres) and especially in the predefined FOV no visual differences to the ground truth are detectable. This is underlined by difference plots in the second row of Fig. 4. The relative error is smaller than 1% everywhere in the FOV and increasing outside the edges regions of convergence. The linearity of the gradient in the center line of the Halbach configuration is showcased on the lower left side. Between -0.15 m and 0.15 m the gradient shows nearly perfect linearity. In this section, all three lines are visually on top of each other. The difference from the harmonic expansion gradients to the ground truth increases on the outer ends (outside the reference ellipsoid and the outer spheres, respectively).

Using the 14-design on the reference ellipsoid for the simulated gradient field, a mean error of $\mathrm{mean}_{\Omega_{\mathrm{FOV}}}(\xi^{\mathrm{grad}}_{\mathrm{EHE}}) = 0.34\%$ and a maximum error of $\max_{\Omega_{\mathrm{FOV}}}(\xi^{\mathrm{grad}}_{\mathrm{EHE}}) = 2.19\%$ have been attained inside the FOV. Again the error increases towards the border of the ellipsoid but remains below 1% for the majority of the FOV. Considering the three shifted spheres with threefold data points for a spherical harmonic expansion, a mean error of

$\text{mean}_{\Omega_{\text{FOV}}}(\xi_{\text{SHE}}^{\text{grad}}) = 0.16\%$ and a maximum error of $\max_{\Omega_{\text{FOV}}}(\xi_{\text{SHE}}^{\text{grad}}) = 2.23\%$ was achieved inside the FOV.

Discussion

Although the geometric form of an ellipsoid can be continuously simplified to a sphere, such a reduction from ellipsoidal to spherical harmonics is not straightforward and unique[53]. However, as shown in the "Methods" section, spherical and ellipsoidal harmonic expansions have great similarities in structure. In both cases, we consider a linear combination of basis functions of harmonic polynomials up to a certain degree on the spherical or ellipsoidal FOV. In both cases we have to solve a surface integral (on the sphere or reference ellipsoid) to obtain the coefficients. These surface integrals can be solved efficiently using *t*-designs. To do this, we use the transformation formula (9) between the two integrals to define ellipsoidal *t*-designs on the reference ellipsoid from their counterparts on the unit sphere. This transformation step is crucial for an efficient calculation of ellipsoidal harmonic expansions and thus enables their use for efficient representation of magnetic fields.

In order to validate the accuracy of the numerical integration using ellipsoidal *t*-designs and — by doing so — to demonstrate the representation of magnetic fields present in tomographic imaging using ellipsoidal harmonic expansions, a permanent magnet Halbach ring array for low-field MRI was considered. In this context, a high length-to-diameter ratio directly correlates with enhanced field homogeneity. This allows the FOV to be efficiently covered by an ellipsoid, thereby underscoring the practical utility of ellipsoidal harmonics. Two ellipsoidal *t*-designs of different sizes were used to emphasize the gain in accuracy with increasing *t*. Three shifted spheres were used for comparison. We considered two spherical *t*-designs, one of them with the same total number of data points compared to the larger ellipsoidal *t*-design. This allows for a direct comparison and highlights

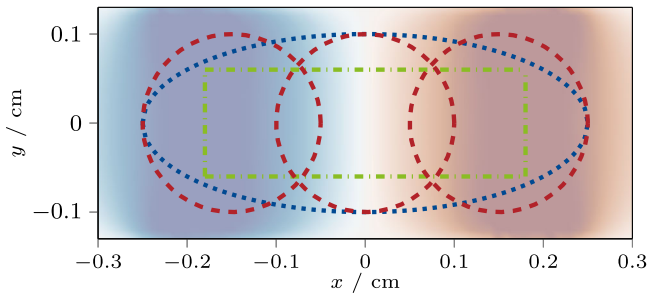

Fig. 2 | Field of view coverage in a gradient field with shifted spheres and ellipsoid. Shown is the central *x*, *y*-plane of an MRI gradient field. The reference ellipsoid (displayed as a blue dotted line) and three shifted spheres (displayed as red dashed lines) are chosen to comprise the field of view of the gradient field (displayed as a green line). The *z*-component of the simulated gradient field is indicated in the background.

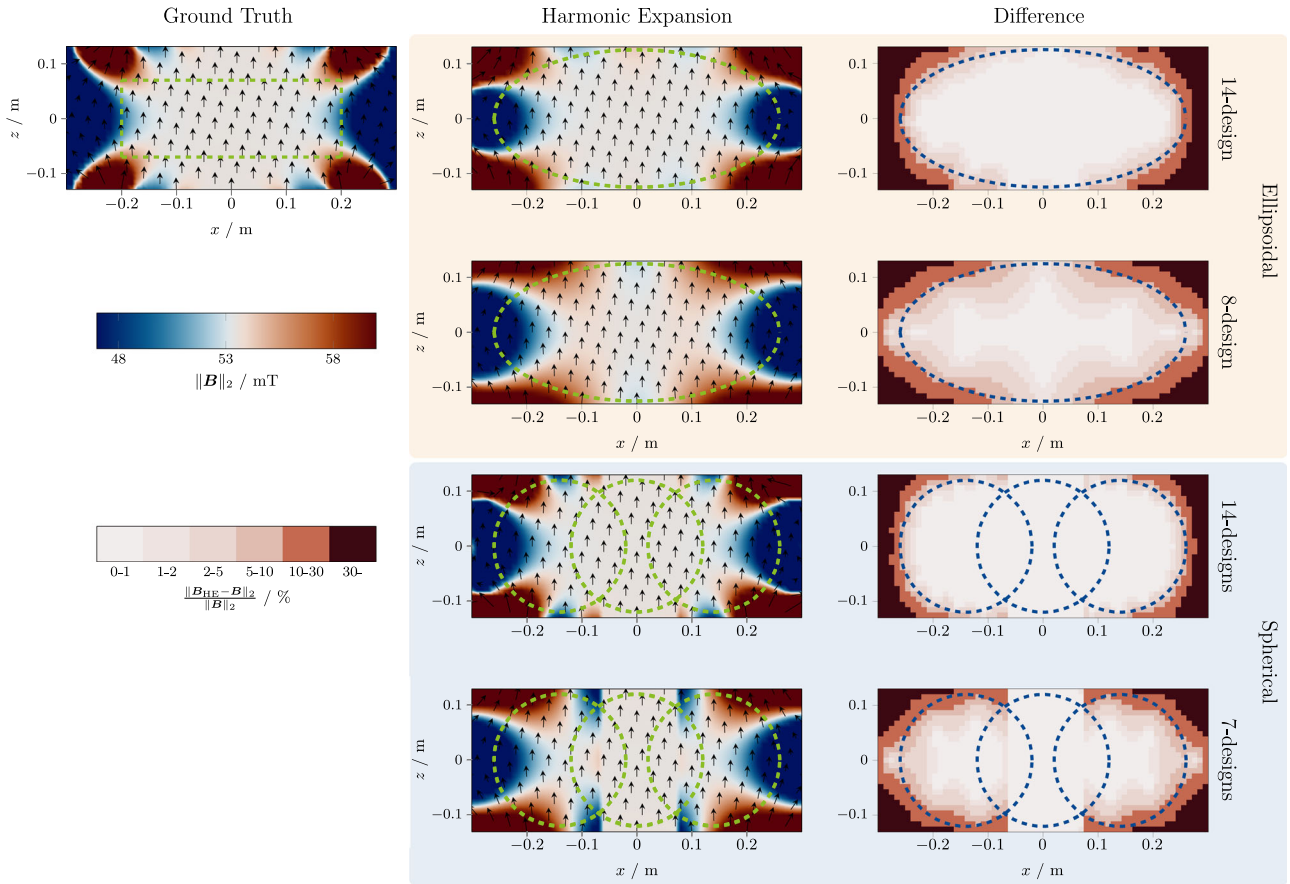

Fig. 3 | Comparison of a simulated MRI B_0 field and its approximation using harmonic expansions. Shown are the experimental results of the B_0-field in the *x*, *z*-plane. The simulated MRI B_0-field is labeled as Ground Truth and includes the cylindrical field of view as green dashed line. The calculated B_0-fields using an ellipsoidal harmonic expansion with a 14-design and a 8-design and spherical harmonic expansions with 14-designs and 7-designs are shown and labeled accordingly. The reference ellipsoid and the spheres are indicated as green dashed lines within the field plots. A joint color bar indicating the absolute field values from 47 mT (dark blue) to 60 mT (dark red) is provided. Moreover, the relative errors (as defined in (1)) to the ground truth are shown for all four cases, labeled as Difference plots. The reference ellipsoid and the spheres are indicated as blue dashed lines within the difference plots. A joint color bar for the difference plots indicating the relative error within six bins from 0 to 1% (light pink) to > 30% (dark red) is provided.

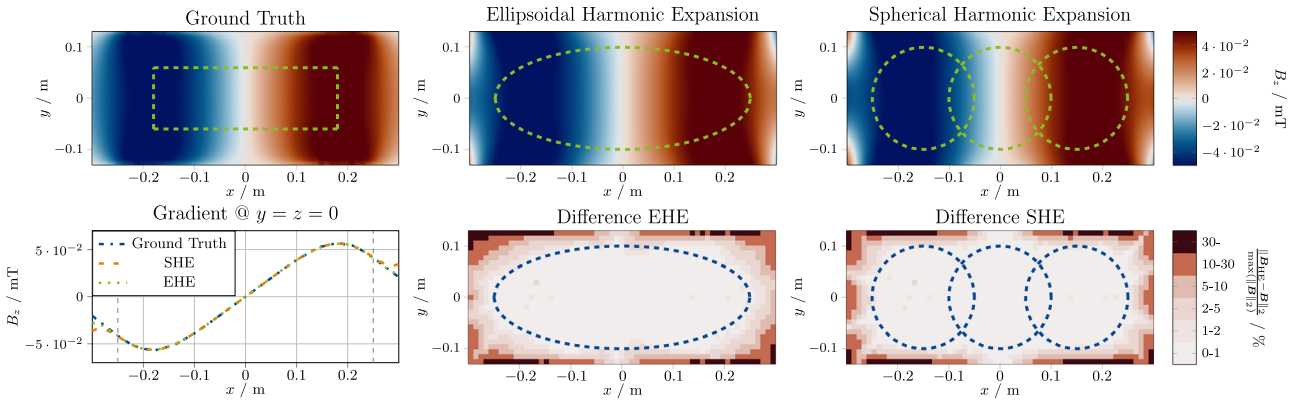

Fig. 4 | Comparison of a simulated MRI gradient field and its approximation using harmonic expansions. Shown are the experimental results of the MRI gradient field in the x, y-plane. The simulated gradient field is labeled as Ground Truth and includes the cylindrical field of view as green dashed line. Heatmaps of the calculated gradient fields using ellipsoidal and spherical harmonics are shown and labeled accordingly. The reference ellipsoid and the spheres are indicated as green dashed lines within the field plots. A joint color bar indicating the z-component of the field values from −0.05 mT (dark blue) to 0.05 mT (dark red) is provided. The relative errors (as defined in (2)) to the ground truth are shown for both cases, labeled as Difference EHE for the ellipsoidal harmonic expansion and Difference SHE for the spherical harmonic expansion. The reference ellipsoid and the spheres are indicated as blue dashed lines within the difference plots. A joint color bar for the difference plots indicating the relative error within six bins from 0 to 1% (light pink) to > 30% (dark red) is provided. Moreover, the B_z values of the ground truth, the spherical harmonic expansion (SHE) and the ellipsoidal harmonic expansion (EHE) at $y = z = 0$ are compared in a separate line-plot labeled as Gradient at $y = z = 0$. The border of the ellipsoid and the spheres in x − *direction* are displayed as gray dashed lines.

the gain in accuracy that can be achieved with ellipsoidal harmonic expansions.

The results presented in subsection "Experimental results: homogeneous field" show that the ellipsoidal harmonic expansion — efficiently computed using an ellipsoidal t-design—is fully capable of recovering the B_0 field. Although a small 8-design with only 44 data points can be interesting to get a first impression of the fields, it produces some inaccuracies. In contrast, the larger 14-design with 114 data points gives a very good result. With a mean error of less than 1% within the FOV, the accuracy is comparable to the field recovered using a spherical harmonic expansion, but requires only a third of the data points. Compared to a spherical harmonic expansion with the same number of data points, the ellipsoidal harmonic expansion achieves a gain in accuracy. For both methods, the error increases in the outer regions of the FOV. This is expected because both expansions converge only within the reference ellipsoid or spheres.

The results on the gradient field presented in subsection "Experimental results: gradient field" corroborate these assertions. The mean error within the reference ellipsoid is notably minimal, falling well below 1%. This is comparable to the mean error obtained using spherical harmonics on the conjunction of three shifted spheres, but again using only a third of the data points. The overall smaller error can be explained by the good linearity of the gradient field within the selected reference ellipsoid and spheres.

It should be noted that for both methods there is also an error in the interpolation of the field values to the points of the corresponding t-design. The results in this paper are based on simulated fields. In actual measurements, there will be discrepancies due to factors such as the accuracy of the robot resulting in small displacements and the accuracy of the magnetometer due to time drifts or measurement noise. The analysis of the total error for real magnetic field measurements remains a subject for future research. However, t-designs represent a very robust quadrature in the context of node displacements and function evaluation.

In general, we can conclude that ellipsoidal harmonic expansions provide a valuable gain for efficient measurement and representation of magnetic fields in tomographic imaging. Two additional degrees of freedom compared to spherical regions provide significant advantages in covering a variety of scanner bores. Therefore, ellipsoidal harmonic expansions should be considered over spherical harmonic expansions whenever the physical dimensions require this geometric flexibility. An effective and accurate calculation of the ellipsoidal coefficients was presented by solving the surface integrals using ellipsoidal t-designs. To this end, the implementation of precise transformations between Cartesian coordinates and ellipsoidal coordinates must be handled carefully, taking into account the sign conventions. To reduce the computational cost, it is mandatory to construct the $(\frac{T}{2}+1)^2$ Lamé functions depending on the selected reference ellipsoid and t-design only once before the field evaluations. The Lamé functions can be computed efficiently by setting up the determinants of matrices up to size $\frac{T^2}{2}$ as defined in subsection "Lamé functions" and finding their roots in a fast way. The Lamé functions can be stored for later evaluation of the fields. A fast implementation in Julia is published alongside the paper. It should be noted that the presented methods and the provided code could also be of great use in other research fields where ellipsoidal harmonics are applied (e.g., chemical physics, fluid dynamics, astrophysics and plasma science).

A comprehensive examination of the measurement and representation of magnetic fields in tomographic imaging employing prolate or oblate spheroidal harmonics is of significant interest. These harmonics provide an intermediate level of flexibility and complexity, situated between spherical and ellipsoidal harmonics. Consequently, this research question serves as a logical starting point for future studies.

The flexibility gained in covering a cylindrical FOV using ellipsoidal harmonic expansions pose a great advantage for high temporal resolution magnetic field measurements. Such measurements provide valuable insight into signal generation, for example in MRI or MPI. A spherical single-shot magnetic field measurement device capable of a measurement rate of 10 Hz has recently been presented[54]. A similar ellipsoidal device could be designed to provide such a measurement rate over a larger non-spherical FOV.

Methods

Spherical harmonics series expansion

Solid real spherical harmonics can be used for an efficient representation of source-free magnetic fields inside an arbitrary spherical volume as follows[32]. Let us consider a ball $\mathcal{B}_R(\boldsymbol{p})$ with arbitrary radius $R \in \mathbb{R}_+$ and center $\boldsymbol{p} \in \mathbb{R}^3$. Further, let the function $f : \mathcal{B}_R(\boldsymbol{p}) \to \mathbb{R}$ fulfill Laplace's equation

with Dirichlet boundary conditions, i.e.,

$$\begin{cases} \Delta f(\boldsymbol{a}) = 0, & \forall \boldsymbol{a} \in \mathcal{B}_R^\circ(\boldsymbol{p}), \\ f(\boldsymbol{a}) = F(\boldsymbol{a}), & \forall \boldsymbol{a} \in \partial\mathcal{B}_R(\boldsymbol{p}), \end{cases}$$

where $F \in C^\infty\left(\partial\mathcal{B}_R(\boldsymbol{p})\right)$. Then f can be represented through

$$f(\boldsymbol{a}) = \sum_{n=0}^{\infty} \sum_{m=-n}^{n} A_S^{n,m}(\boldsymbol{p}, R)\left(\frac{1}{R}\right)^n Z_n^m(\boldsymbol{a}-\boldsymbol{p}) \forall \boldsymbol{a} \in \mathcal{B}_R(\boldsymbol{p}), \tag{3}$$

where the spherical coefficients are calculated on the unit sphere via

$$A_S^{n,m}(\boldsymbol{p}, R) = \oint_{\mathbb{S}^2} F(R\boldsymbol{a}+\boldsymbol{p}) Z_n^m(\boldsymbol{a})\, \mathrm{d}\boldsymbol{a}, \tag{4}$$

and the normalized real solid spherical harmonics are given as

$$Z_n^m : \mathbb{R}^3 \to \mathbb{R}, (r, \vartheta, \varphi) \mapsto \gamma_S^{n,|m|} r^n P_n^{|m|}(\cos\vartheta) \begin{cases} \sqrt{2}\cos m\varphi, & m > 0, \\ \sqrt{2}\sin|m|\varphi, & m < 0, \\ 1, & m = 0. \end{cases} \tag{5}$$

Here, P_n^m are the associated Legendre polynomials and $\gamma_S^{n,|m|} = \sqrt{\frac{2n+1}{4\pi}\frac{(n-m)!}{(n+m)!}}$ is the spherical normalization factor.

If f is a polynomial of maximum degree $N \in \mathbb{N}$, the outer sum in Eq. (3) can be truncated to $n \in \{0, 1, \ldots, N\}$. Since we assume that the magnetic field $\boldsymbol{B} : \mathcal{B}_R(\boldsymbol{p}) \to \mathbb{R}^3$ inside the chosen ball, its components can be described by a harmonic polynomial of maximum degree $N \in \mathbb{N}$ and thus $N+1$ summands in the outer sum are sufficient for an exact spherical harmonic expansion. Furthermore, following[32], the spherical coefficients $A_S^{n,m}$ can be calculated exactly by using a spherical t-design $\{\boldsymbol{y}_i\}$ with $L \in \mathbb{N}$ nodes $\boldsymbol{y}_i \in \mathbb{S}^2$ and $i \in \{0, \ldots, L-1\}$ for $t \geq 2N$.

Ellipsoidal harmonics series expansion

The objective of the following sections is to extend the considerations of the last section to ellipsoids. For a detailed reference work on ellipsoidal harmonics we refer to[53]. Let us now consider a region of ellipsoidal shape $\Omega \subset \mathbb{R}^3$, called reference ellipsoid. The reference ellipsoid is defined by its three semi-axes $0 < a_3 < a_2 < a_1$ via

$$\frac{x^2}{a_1^2} + \frac{y^2}{a_2^2} + \frac{z^2}{a_3^2} = 1. \tag{6}$$

A reference ellipsoid with its semi-axes is visualized in Fig. 5.

The linear eccentricities of the reference ellipsoid are given as

$$h_1 = \sqrt{(a_2^2 - a_3^2)}, \quad h_2 = \sqrt{(a_1^2 - a_3^2)}, \quad h_3 = \sqrt{(a_1^2 - a_2^2)}. \tag{7}$$

In order to describe the Laplace's partial differential equation inside the reference ellipsoid, we introduce an orthogonal ellipsoidal coordinate system ρ, μ, ν. A proper definition of ρ, μ, ν and the connection to Cartesian coordinates can be found in subsection "Ellipsoidal coordinates".

Let the function $f : \Omega \to \mathbb{R}$ fulfill Laplace's equation inside the reference ellipsoid, i.e.,

$$\begin{cases} \Delta f(\rho, \mu, \nu) = 0, & h_2 \leq \rho < a_1, \\ f(\rho, \mu, \nu) = F(\mu, \nu), & \rho = a_1, \end{cases}$$

where $F \in C^\infty(S_{a_1})$ and S_{a_1} describes the surface of the reference ellipsoid.

Expressing Laplace's equation inside the reference ellipsoid in ellipsoidal coordinates and using a separation of variables leads to the Lamé equation. Solutions of this equation are the so called Lamé functions $E_n^m : \mathbb{R} \to \mathbb{R}$ with degree $n \in \mathbb{N}$ and order $m \in \{1, \ldots, 2n+1\}$. The exact definitions are given in more detail in subsection "Lamé functions".

With the Lamé functions at hand, we consider the inner ellipsoidal harmonics

$$\mathbb{E}_n^m(\rho, \mu, \nu) = E_n^m(\rho) E_n^m(\mu) E_n^m(\nu), \tag{8}$$

which form a basis of the harmonic polynomials of degree $n \leq N, N \in \mathbb{N}$ (more details are given in subsection "Ellipsoidal harmonics").

It follows, that

$$f(\rho, \mu, \nu) = \sum_{n=0}^{\infty} \sum_{m=1}^{2n+1} A_{a_1}^{n,m} \mathbb{E}_n^m(\rho, \mu, \nu), \tag{9}$$

and on the boundary

$$F(\mu, \nu) = \sum_{n=0}^{\infty} \sum_{m=1}^{2n+1} A_{a_1}^{n,m} E_n^m(a_1) S_n^m(\mu, \nu). \tag{10}$$

$S_n^m(\mu, \nu) = E_n^m(\mu) E_n^m(\nu)$ are the so-called surface ellipsoidal harmonics and the coefficients $A_{a_1}^{n,m} \in \mathbb{R}$ are obtained from their orthogonality via

$$A_{a_1}^{n,m} = \frac{1}{\gamma_{a_1}^{n,m} E_n^m(a_1)} \oint_{S_{a_1}} F(\mu, \nu) S_n^m(\mu, \nu)\, \mathrm{d}\Omega(\mu, \nu), \tag{11}$$

with the ellipsoidal normalization factor $\gamma_{a_1}^{n,m}$ as defined in subsection "Ellipsoidal harmonics".

Furthermore, if f is a polynomial of maximum degree $N \in \mathbb{N}$, the outer sums in Eqs. (9) and (10) can be truncated to $n \in \{0, 1, \ldots, N\}$.

Quadrature on ellipsoidal surface

In order to solve the surface integrals in Eqs. (11) and (30) numerically, we consider the following transformation-formula between integrals on ellipsoidal surfaces and spheres

$$\oint_{S_{a_1}} F(\mu, \nu)\, \mathrm{d}\Omega(\mu, \nu) = \int_0^{2\pi} \int_0^{\pi} F(\mu(\vartheta_e, \varphi_e), \nu(\vartheta_e, \varphi_e)) \sin\vartheta_e\, \mathrm{d}\vartheta_e\, \mathrm{d}\varphi_e, \tag{12}$$

where F is defined on the surface of the reference ellipsoid and $\vartheta_e \in [0, \pi], \varphi_e \in [0, 2\pi)$ are so-called elliptospherical coordinates (see chapter 6 in[53]). We consider a spherical t-design $\{\boldsymbol{y}_i\}$[55] with $L \in \mathbb{N}$ nodes $\boldsymbol{y}_i \in \mathbb{S}^2$ and $i \in \{0, \ldots, L-1\}$, i.e., for a polynomial g on the unit sphere with maximum degree $t \in \mathbb{N}$ it holds, that

$$\oint_{\mathbb{S}^2} g(\boldsymbol{y})\, \mathrm{d}\Omega = \frac{4\pi}{L} \sum_{i=0}^{L-1} g(\boldsymbol{y}_i).$$

In particular, if we consider g such that $F(\mu(\vartheta_e, \varphi_e), \nu(\vartheta_e, \varphi_e)) = g(\vartheta_e, \varphi_e)$ it follows, that

$$\begin{aligned} \oint_{S_{a_1}} F(\mu, \nu)\, \mathrm{d}\Omega(\mu, \nu) &= \int_0^{2\pi} \int_0^{\pi} F(\mu(\vartheta_e, \varphi_e), \nu(\vartheta_e, \varphi_e)) \sin\vartheta_e\, \mathrm{d}\vartheta_e\, \mathrm{d}\varphi_e \\ &= \int_0^{2\pi} \int_0^{\pi} g(\vartheta_e, \varphi_e) \sin\vartheta_e\, \mathrm{d}\vartheta_e\, \mathrm{d}\varphi_e = \frac{4\pi}{L} \sum_{i=0}^{L-1} g(\boldsymbol{y}_i), \end{aligned}$$

and F is a polynomial with maximum degree $t \in \mathbb{N}$ on the ellipsoidal surface, if and only if g is a polynomial with maximum degree $t \in \mathbb{N}$ on the unit sphere. Here, the angular coordinates ϑ_e, φ_e can be transformed into

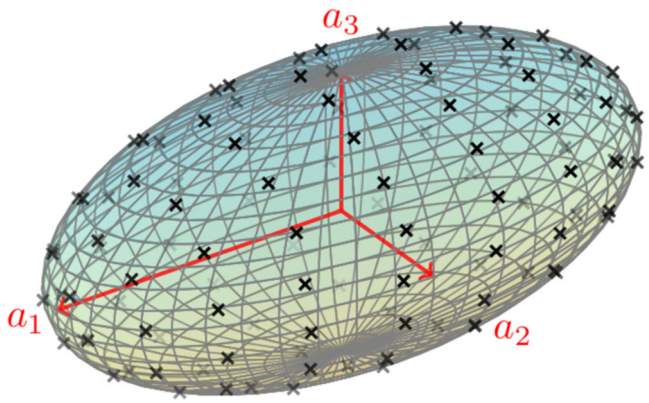

Fig. 5 | Reference ellipsoid with ellipsoidal *t*-design. Shown is a reference ellipsoid defined by its semi-axes $0 < a_3 < a_2 < a_1$ displayed as red arrows. Furthermore, the measurement points of an ellipsoidal *t*-design (with $t = 14$) are indicated as crosses on the ellipsoidal surface.

Cartesian coordinates on the unit sphere using

$$(y_1, y_2, y_3) = \left(\sin(\vartheta_e)\cos(\varphi_e), \sin(\vartheta_e)\sin(\varphi_e), \cos(\vartheta_e)\right)$$

and further into Cartesian coordinates on the ellipsoidal surface using

$$(x_1, x_2, x_3) = \left(y_3\rho, y_1\sqrt{\rho^2 - h_3^2}, y_2\sqrt{\rho^2 - h_2^2}\right).$$

Using this coordinate transformation on the spherical *t*-design $\{\boldsymbol{y}_i\} \subset \mathbb{S}^2$, we get points $\{\boldsymbol{x}_i\} \subset S_{a_1}$ on the ellipsoidal surface. Since $F(\boldsymbol{x}_i) = g(\boldsymbol{y}_i)$ follows directly from $F(\mu(\vartheta_e, \varphi_e), \nu(\vartheta_e, \varphi_e)) = g(\vartheta_e, \varphi_e)$, $\{\boldsymbol{x}_i\}$ poses an ellipsoidal *t*-design, i.e.,

$$\oint_{S_{a_1}} F(\mu, \nu)\, \mathrm{d}\Omega(\mu, \nu) = \frac{4\pi}{L}\sum_{i=0}^{L-1} F(\boldsymbol{x}_i).$$

As a result of these considerations, $\gamma_{a_1}^{n,m}$ and A_n^m can be calculated exactly using an ellipsoidal *t*-design with $t \geq 2n$.

Despite the fact that quadratures using a *t*-design are exact for integrals over polynomials with maximal degree *t*, the robustness of such quadratures is primarily contingent on disturbances in the node positions and errors in the function evaluation at these positions. The first point is often addressed by introducing small neighborhoods around the node positions in which the design remains a positive quadrature rule. The determination of upper limits for the radius of these neighborhoods remains an active area of research[56,57]. An important property of a *t*-design is the uniformity of its quadrature weights, which makes it particularly robust to perturbations in node positions compared to other quadratures. The evaluation of the function is subject to uncertainty due to measurement and interpolation errors. Furthermore, the consideration of functions as polynomials is often subject to specific assumptions. However, upper limits for the quadrature error do exist for continuously differentiable functions. The error diminishes with increasing smoothness of the functions under consideration and larger values of *t*[58].

Efficient calculation of source-free magnetic fields

As mentioned above, the magnetic fields inside the bore of MRI scanners can be assumed to be harmonic. We consider an ellipsoidal region $\Omega \subset \mathbb{R}^3$ inside the bore and define the semi-axes of the reference ellipsoid accordingly. Further, we assume that the magnetic field $\boldsymbol{B} : \Omega \to \mathbb{R}^3$ can be described by a harmonic polynomial of maximum degree $N \in \mathbb{N}$

$$\boldsymbol{B}(\rho, \mu, \nu) = \sum_{n=0}^{N}\sum_{m=1}^{2n+1} \boldsymbol{A}_{a_1}^{n,m}\mathbb{E}_n^m(\rho, \mu, \nu). \tag{13}$$

Considering an ellipsoidal *t*-design $\{\boldsymbol{x}_i\}$ with $t \geq 2N$ we transform the $L \in \mathbb{N}$ nodes into ellipsoidal coordinates (ρ, μ, ν) using the transformation given in subsection "Ellipsoidal coordinates". After obtaining an ellipsoidal *t*-design in ellipsoidal coordinates $\{(\rho_i, \mu_i, \nu_i)\}$, the coefficients $\boldsymbol{A}_{a_1}^{n,m}$ can be calculated exactly via

$$\boldsymbol{A}_{a_1}^{n,m} = \frac{4\pi}{L\gamma_{a_1}^{n,m}E_n^m(a_1)}\sum_{i=0}^{L-1}\boldsymbol{B}(\rho_i, \mu_i, \nu_i)S_n^m(\mu_i, \nu_i), \tag{14}$$

$$\gamma_{a_1}^{n,m} = \frac{4\pi}{L}\sum_{i=0}^{L-1}\left(S_n^m(\mu_i, \nu_i)\right)^2. \tag{15}$$

Ellipsoidal coordinates

In this section we give a proper definition of the ellipsoidal coordinates ρ, μ, ν, in which the Laplace partial differential equation can be decomposed into separable functions. This definition is based on the work presented in ref. 53. Moreover, using ellipsoidal coordinates ρ, μ, ν, the surface of a triaxial ellipsoid can be expressed easily in comparison to Cartesian coordinates. However, integration schemes are commonly given in Cartesian coordinates. Thus, analytical conversion between the coordinate systems is crucial and thus also given below.

For a parameter $s \in \mathbb{R}$, a family of confocal quadrics based on the reference ellipsoid (6) is given by

$$\frac{x^2}{a_1^2 + s} + \frac{y^2}{a_2^2 + s} + \frac{z^2}{a_3^2 + s} = 1, \tag{16}$$

and especially, when $-a_3^2 < s < \infty$, (16) represents a triaxial ellipsoid. For every point (x, y, z) with $xyz \neq 0$, (16) is a cubic equation in s with three real roots (see chapter 1 in ref. 53)

$$-a_1^2 < s_3 < -a_2^2 < s_2 < -a_3^2 < s_1 < \infty,$$

defining an ellipsoidal coordinate system. Now, we can introduce ellipsoidal coordinates with dimension of length (ρ, μ, ν) by

$$s_1 = \rho^2 - a_1^2, \quad s_2 = \mu^2 - a_1^2, \quad s_3 = \nu^2 - a_1^2. \tag{17}$$

Given a point in these ellipsoidal coordinates, the corresponding Cartesian coordinates can be calculated with the following connection formula[46,59,60]

$$\begin{aligned} x &= \frac{1}{h_2h_3}\rho\mu\nu, \\ y &= \frac{1}{h_1h_3}\sqrt{\rho^2 - h_3^2}\sqrt{\mu^2 - h_3^2}\sqrt{h_3^2 - \nu^2}, \\ z &= \frac{1}{h_2h_1}\sqrt{\rho^2 - h_2^2}\sqrt{h_2^2 - \mu^2}\sqrt{h_2^2 - \nu^2}, \end{aligned} \tag{18}$$

where $0 \leq \nu \leq h_3 \leq \mu \leq h_2 \leq \rho < \infty$ and $\mathrm{sign}(x) = \mathrm{sign}(\nu)$, $\mathrm{sign}(y) = \mathrm{sign}(\sqrt{h_3^2 - \nu^2})$, $\mathrm{sign}(z) = \mathrm{sign}(\sqrt{h_2^2 - \mu^2})$ and h_1, h_2, h_3 as in (7). Thus, to fully fix a Cartesian coordinate in space, we need to store the signs next to the values of ρ, μ and ν.

To obtain the ellipsoidal coordinates given Cartesian coordinates, we start by substituting the system (18) into (16) and get the cubic equation

$$s^3 + c_2 s^2 + c_1 s + c_0 = 0$$

where

$$\begin{aligned} c_2 &= a_1^2 + a_2^2 + a_3^2 - x^2 - y^2 - z^2, \\ c_1 &= a_1^2 a_2^2 + a_1^2 a_3^2 + a_2^2 a_3^2 \\ &\quad - (a_2^2 + a_3^2)x^2 - (a_1^2 + a_3^2)y^2 - (a_1^2 + a_2^2)z^2, \\ c_0 &= a_1^2 a_2^2 a_3^2 - a_2^2 a_3^2 x^2 - a_1^2 a_3^2 y^2 - a_1^2 a_2^2 z^2. \end{aligned}$$

This equation has the three real roots

$$\begin{aligned} s_1 &= 2\sqrt{p}\cos\left(\frac{\omega}{3}\right) - \frac{c_2}{3}, \\ s_2 &= 2\sqrt{p}\cos\left(\frac{\omega}{3} - \frac{2\pi}{3}\right) - \frac{c_2}{3}, \\ s_3 &= 2\sqrt{p}\cos\left(\frac{\omega}{3} - \frac{4\pi}{3}\right) - \frac{c_2}{3}, \end{aligned}$$

where

$$\begin{aligned} \omega &= \begin{cases} \arccos\left(\frac{q}{p^{3/2}}\right), & \text{for } q < p^{3/2}, \\ 0, & \text{for } q \geq p^{3/2}, \end{cases} \\ p &= \frac{c_2^2 - 3c_1}{9}, \\ q &= \frac{9c_1c_2 - 27c_0 - 2c_2^3}{54}. \end{aligned}$$

Using Eq. (17) we can calculate ρ, μ, ν while take into account the above sign conventions.

A family of ellipsoids in ellipsoidal coordinates is given by

$$\frac{x^2}{\rho^2} + \frac{y^2}{\rho^2 - h_3^2} + \frac{z^2}{\rho^2 - h_2^2} = 1.$$

For a given reference ellipsoid (a_1, a_2, a_3), a constant $\rho \in (h_2, \infty)$ describes the surface of an ellipsoid from that family and especially by setting $\rho = a_1$ the surface of the reference ellipsoid.

Lamé functions

This section is based on the work[53].

Lamé functions can be divided in four classes

$$\begin{aligned} \mathcal{K} &= \{P(\chi)\}, \\ \mathcal{L} &= \{\sqrt{|\chi^2 - h_3^2|}P(\chi)\}, \\ \mathcal{M} &= \{\sqrt{|\chi^2 - h_2^2|}P(\chi)\}, \\ \mathcal{N} &= \{\sqrt{|\chi^2 - h_3^2|}\sqrt{|\chi^2 - h_2^2|}P(\chi)\}, \end{aligned}$$

where $P(\chi) = a_0\chi^n + a_1\chi^{n-2} + \ldots + a_k\chi^{n-2k} + \ldots$ is a polynomial of maximum degree n, $a_k \in \mathbb{R}$ and $\chi \in \{\rho, \mu, \nu\}$. There are always $2n + 1$ linearly independent Lamé functions of degree n, distributed over the four classes and sorted using the index $m = 1, \ldots, 2n + 1$. Developing the Lamé functions of degree n for a given reference ellipsoid is an $\mathcal{O}(n^3)$ problem for all four classes, presented in[53]. The prefactors of the classes $\mathcal{L}, \mathcal{M}$ and $\mathcal{N}$ involve square roots where the sign conventions need to be respected for $x = \mu$ and $x = \nu$, but the polynomial parts remain the same.

We follow the derivations in chapter 3 of ref. 53 for the calculations of the Lamé functions. Let $\alpha = h_3^2 + h_2^2$ and $\beta = h_3^2 h_2^2$.

Lamé functions in class $\mathcal{K}$. Lamé functions of class $\mathcal{K}$ and degree $n \in \mathbb{N}$ have the form

$$K_n(\chi) = \sum_{k=0}^{\infty} a_k \chi^{n-2k} \tag{19}$$

with coefficients $a_k \in \mathbb{R}$ and $\chi \in \{\rho, \mu, \nu\}$. We define

$$r = \begin{cases} \frac{n}{2}, & \text{for } n \text{ even}, \\ \frac{n-1}{2}, & \text{for } n \text{ odd}. \end{cases}$$

When substituting Eq. (19) into the Lamé equation, the following algebraic system can be found

$$\begin{aligned} 2(k+2)(2n-2k-1)a_{k+1} &= \alpha\left[p - (n-2k)^2\right]a_k \\ &\quad + \beta(n-2k+2)(n-2k+1)a_{k-1}, \end{aligned} \tag{20}$$

for $k \in \{0, \ldots, r\}$ and initial coefficients $a_0 = 1$, $a_{-1} = 0$. Moreover, it holds, that $\forall k \geq r + 1$: $a_k = 0$. For Eq. (20) non-trivial solutions exist for $r + 1$ different constants p. These constants can be determined by solving

$$\begin{vmatrix} K_{1,1} & K_{1,2} & 0 & \ldots & & & 0 \\ K_{2,1} & K_{2,2} & K_{2,3} & \ddots & & & \vdots \\ 0 & K_{3,2} & K_{3,3} & \ddots & & & \\ \vdots & \ddots & \ddots & \ddots & & & \\ & & & & K_{r-1,r-1} & K_{r-1,r} & 0 \\ & & & & K_{r,r-1} & K_{r,r} & K_{r,r+1} \\ 0 & \ldots & & & 0 & K_{r+1,r} & K_{r+1,r+1} \end{vmatrix} = 0,$$

where

$$\begin{aligned} K_{j,j} &= -\alpha\left[p - (n-2j+2)^2\right] \text{ for } j \in \{1, \ldots, r+1\} \\ K_{j,j+1} &= 2j(2n-2j+1), \text{ for } j \in \{1, \ldots, r\} \\ K_{j+1,j} &= -\beta(n-2j+1)(n-2j+2), \text{ for } j \in \{1, \ldots, r\}. \end{aligned} \tag{21}$$

For each of the $r + 1$ solutions p, $r + 1$ coefficients a_k can be calculated recursively and we thus obtain $r + 1$ Lamé functions of class $\mathcal{K}$ and degree n.

Lamé functions in classes $\mathcal{L}$ and $\mathcal{M}$. Lamé functions of class $\mathcal{L}$ and degree $n \in \mathbb{N}$ have the form $L_n(\chi) = \sqrt{|\chi^2 - h_3^2|}P_{n-1}(\chi)$, where

$$P_{n-1}(\chi) = \sum_{k=0}^{\infty} b_k \chi^{n-1-2k} \tag{22}$$

with coefficients $b_k \in \mathbb{R}$ and $\chi \in \{\rho, \mu, \nu\}$. Note, that the sign convention needs to be respected for the non-polynomial part when evaluating for $\chi = \nu$. We define

$$r = \begin{cases} \frac{n}{2}, \text{ for } n \text{ even}, \\ \frac{n+1}{2}, \text{ for } n \text{ odd}. \end{cases}$$

When substituting Eq. (22) into the Lamé equation, the following algebraic system can be found

$$\begin{aligned}2(k+1)(2n-2k-1)b_{k+1} =& \left(\alpha\left[p-(n-2k-1)^2\right]\right.\\ &\left.-(2n-4k-1)h_2^2\right)b_k\\ &+\beta(n-2k+1)(n-2k)b_{k-1},\end{aligned} \tag{23}$$

for $k \in \{0, \ldots, r-1\}$ and initial coefficients $b_0 = 1$, $b_{-1} = 0$. Moreover, it holds, that $\forall k \geq r$: $b_k = 0$. For Eq. (23) non-trivial solutions exist for r different constants p. These constants can be determined by solving

$$\begin{vmatrix} L_{1,1} & L_{1,2} & 0 & \ldots & & & 0 \\ L_{2,1} & L_{2,2} & L_{2,3} & \ddots & & & \vdots \\ 0 & L_{3,2} & L_{3,3} & \ddots & & & \\ \vdots & \ddots & \ddots & \ddots & & & \\ & & & & L_{r-2,r-2} & L_{r-2,r-1} & 0 \\ & & & & L_{r-1,r-2} & L_{r-1,r-1} & L_{r-1,r} \\ 0 & \ldots & & & 0 & L_{r,r-1} & L_{r,r} \end{vmatrix} = 0,$$

where

$$\begin{aligned} L_{j,j} &= -\alpha\left[p-(n-2j+1)^2\right]+(2n-4j+4)h_2^2, \\ &\quad \text{for } j \in \{1,\ldots,r\} \\ L_{j,j+1} &= 2j(2n-2j+1), \text{ for } j \in \{1,\ldots,r-1\} \\ L_{j+1,j} &= -\beta(n-2j+1)(n-2j), \text{ for } j \in \{1,\ldots,r-1\}. \end{aligned} \tag{24}$$

With r solutions p the coefficients b_k can be calculated and we obtain r Lamé functions of class $\mathcal{L}$ and degree n.

Lamé functions of class $\mathcal{M}$ and degree $n \in \mathbb{N}$ have the form $M_n(\chi) = \sqrt{|\chi^2 - h_2^2|}P_{n-1}(\chi)$. Here, the sign convention needs to be respected for the non-polynomial part when evaluating for $\chi = \mu$. The calculation of the coefficients b_k is similar to class $\mathcal{L}$, but h_2^2 needs to be replaced with h_3^2 in Eqs. (23) and (24).

Lamé functions in class $\mathcal{N}$. Lamé functions of class $\mathcal{N}$ and degree $n \in \mathbb{N}$ have the form $N_n(\chi) = \sqrt{|\chi^2 - h_3^2|}\sqrt{|\chi^2 - h_2^2|}P_{n-2}(\chi)$, where

$$P_{n-2}(\chi) = \sum_{k=0}^{\infty} c_k \chi^{n-2-2k} \tag{25}$$

with coefficients $c_k \in \mathbb{R}$ and $\chi \in \{\rho, \mu, \nu\}$. Note, that the sign convention needs to be respected for the non-polynomial part when evaluating for $\chi = \nu$ and $\chi = \mu$. We define

$$r = \begin{cases} \frac{n}{2}, \text{ for } n \text{ even}, \\ \frac{n-1}{2}, \text{ for } n \text{ odd}. \end{cases}$$

When substituting Eq. (25) into the Lamé equation, the following algebraic system can be found

$$\begin{aligned}2(k+1)(2n-2k-1)c_{k+1} =& \alpha\left[p-(n-2k-1)^2\right]c_k\\ &+\beta(n-2k-1)(n-2k)c_{k-1},\end{aligned} \tag{26}$$

for $k \in \{0, \ldots, r-1\}$ and initial coefficients $c_0 = 1$, $c_{-1} = 0$. Moreover, it holds, that $\forall k \geq r$: $c_k = 0$. For Eq. (26) non-trivial solutions exist for r different constants p. These constants can be determined by solving

$$\begin{vmatrix} N_{1,1} & N_{1,2} & 0 & \ldots & & & 0 \\ N_{2,1} & N_{2,2} & N_{2,3} & \ddots & & & \vdots \\ 0 & N_{3,2} & N_{3,3} & \ddots & & & \\ \vdots & \ddots & \ddots & \ddots & & & \\ & & & & N_{r-2,r-2} & N_{r-2,r-1} & 0 \\ & & & & N_{r-1,r-2} & N_{r-1,r-1} & N_{r-1,r} \\ 0 & \ldots & & & 0 & N_{r,r-1} & N_{r,r} \end{vmatrix} = 0,$$

where

$$\begin{aligned} N_{j,j} &= -\alpha\left[p-(n-2j+1)^2\right], \text{ for } j \in \{1,\ldots,r\} \\ N_{j,j+1} &= 2j(2n-2j+1), \text{ for } j \in \{1,\ldots,r-1\} \\ N_{j+1,j} &= -\beta(n-2j-1)(n-2j), \text{ for } j \in \{1,\ldots,r-1\}. \end{aligned} \tag{27}$$

With these r solutions p the coefficients c_k can be calculated and we obtain r Lamé functions of class $\mathcal{N}$ and degree n.

Ellipsoidal harmonics

This section is based on the work[53].

After calculation of the Lamé functions, the inner ellipsoidal harmonics $\mathbb{E}_n^m$ can be derived as the product of the Lamé functions evaluated at the ellipsoidal coordinates

$$\mathbb{E}_n^m(\rho,\mu,\nu) = E_n^m(\rho)E_n^m(\mu)E_n^m(\nu). \tag{28}$$

It is shown in[53], that $\mathbb{E}_n^m$ are harmonic polynomials. It follows directly, that $\{\mathbb{E}_n^m : n \leq N\}$ for $N \in \mathbb{N}$ is a set with $[2N+1] + [2(N-1)+1] + \ldots + [2(1)+1] + [1] = (N+1)^2$ linearly independent elements and a subset of the set of harmonic polynomials. Since the space of harmonic polynomials with degree $n \leq N$ has the dimension $(N+1)^2$, it follows that $\{\mathbb{E}_n^m : n \leq N\}$ is a maximal linear independent subset and thus a basis of the harmonic polynomials of degree $n \leq N$.

Furthermore, we define surface ellipsoidal harmonics S_n^m as

$$S_n^m(\mu,\nu) = E_n^m(\mu)E_n^m(\nu), \tag{29}$$

recalling, that $\rho = a_1$ holds on the surface of the reference ellipsoid S_{a_1}. It follows, that also $E_n^m(\rho) = E_n^m(a_1)$ is a constant on the ellipsoid surface and thus $S_n^m(\mu,\nu) = \mathbb{E}_n^m(a_1,\mu,\nu)/E_n^m(a_1)$ is a polynomial with maximum degree n. In ref. 53 it is shown, that the surface ellipsoidal harmonics are orthogonal to each other with normalization constants $\gamma_{a_1}^{n,m} \in \mathbb{R}$ given via

$$\gamma_{a_1}^{n,m} = \oint_{S_{a_1}} \left(S_n^m(\mu,\nu)\right)^2 \mathrm{d}\Omega(\mu,\nu). \tag{30}$$

Data availability

The data that support the findings of this study are available from the corresponding author upon reasonable request.

Code availability

The implementation of the ellipsoidal harmonic expansion was written in Julia and is published under the MIT License at https://github.com/IBIResearch/EllipsoidalHarmonicExpansions.

Received: 21 October 2024; Accepted: 20 February 2025;
Published online: 22 March 2025

References

1. Nelson, B. J., Kaliakatsos, I. K. & Abbott, J. J. Microrobots for minimally invasive medicine. *Annu. Rev. Biomed. Eng.* **12**, 55–85 (2010).
2. Bente, K., Codutti, A., Bachmann, F. & Faivre, D. Biohybrid and bioinspired magnetic microswimmers. *Small* **14**, 1–25 (2018).
3. Ceylan, H., Yasa, I. C., Kilic, U., Hu, W. & Sitti, M. Translational prospects of untethered medical microrobots. *Prog. Biomed. Eng.* **1**, 012002 (2019).
4. Liu, D., Guo, R., Wang, B., Hu, J. & Lu, Y. Magnetic micro/nanorobots: a new age in biomedicines. *Adv. Intell. Syst.* **4**, 2200208 (2022).
5. Gleich, B., Schmale, I., Nielsen, T. & Rahmer, J. Miniature magneto-mechanical resonators for wireless tracking and sensing. *Science* **380**, 966–971 (2023).
6. Zhou, J. et al. System integration of magnetic medical microrobots: from design to control. *Front. Robot. AI* **10**, 1–10 (2023).
7. Von Arx, D. et al. Simultaneous localization and actuation using electromagnetic navigation systems. *IEEE Trans. Robot.* **40**, 1292–1308 (2024).
8. Dreyfus, R. et al. Dexterous helical magnetic robot for improved endovascular access. *Sci. Robot.* **9**, eadh0298 (2024).
9. Sohail, A., Ahmad, Z., Bég, O. A., Arshad, S. & Sherin, L. A review on hyperthermia via nanoparticle- mediated therapy. *Bull. Cancer* **104**, 452–461 (2017).
10. Peiravi, M., Eslami, H., Ansari, M. & Zare-Zardini, H. Magnetic hyperthermia: potentials and limitations. *J. Indian Chem. Soc.* **99**, 100269 (2022).
11. Mukhatov, A., Le, T., Pham, T. T. & Do, T. D. A comprehensive review on magnetic imaging techniques for biomedical applications. *Nano Sel.* **4**, 213–230 (2023).
12. Liebl, M. et al. Magnetorelaxometry procedures for quantitative imaging and characterization of magnetic nanoparticles in biomedical applications. *Biomed. Eng./Biomed. Tech.* **60**, 427–443 (2015).
13. Rahmer, J., Weizenecker, J., Gleich, B. & Borgert, J. Signal encoding in magnetic particle imaging: properties of the system function. *BMC Med. imaging* **9**, 1–21 (2009).
14. Schultz, G. *Magnetic Resonance Imaging with Nonlinear Gradient Fields: Signal Encoding and Image Reconstruction* (Springer Science & Business Media, 2013).
15. Marques, J. P., Simonis, F. F. & Webb, A. G. Low-field MRI: an MR physics perspective. *J. Magn. Reson. Imaging* **49**, 1528–1542 (2019).
16. Gach, H. M. B0 field homogeneity recommendations, specifications, and measurement units for MRI in radiation therapy. *Med Phys.* **47**, 4101–4114 (2020).
17. Wenzel, K. et al. B0-shimming methodology for affordable and compact low-field magnetic resonance imaging magnets. *Front. Phys.* **9**, 1–12 (2021).
18. Mesri, H. Y., David, S., Viergever, M. A. & Leemans, A. The adverse effect of gradient nonlinearities on diffusion mri: from voxels to group studies. *NeuroImage* **205**, 116127 (2020).
19. Graeser, M. et al. Towards picogram detection of superparamagnetic iron-oxide particles using a gradiometric receive coil. *Sci. Rep.* **7**, 6872 (2017).
20. Foerger, F. et al. Flexible selection field generation using iron core coil arrays. *Int. J. Mag. Part. Imag.* **9**, 2303023 (2023).
21. Sutton, B. P., Noll, D. C. & Fessler, J. A. Fast, iterative image reconstruction for mri in the presence of field inhomogeneities. *IEEE Trans. Med. Imaging* **22**, 178–188 (2003).
22. Eggers, H., Knopp, T. & Potts, D. Field inhomogeneity correction based on gridding reconstruction for magnetic resonance imaging. *IEEE Trans. Med. Imaging* **26**, 374–384 (2007).
23. Knopp, T., Eggers, H., Dahnke, H., Prestin, J. & Sénégas, J. Iterative off-resonance and signal decay correction for improved multi-echo imaging in mri. *IEEE Trans. Med Imaging* **28**, 394–404 (2009).
24. Lacroix, M. et al. Correction for magnetic field inhomogeneities and normalization of voxel values are needed to better reveal the potential of mr radiomic features in lung cancer. *Front. Oncol.* **10**, 43 (2020).
25. Dubovan, P. I., Gilbert, K. M. & Baron, C. A. A correction algorithm for improved magnetic field monitoring with distal field probes. *Magn. Reson. Med.* **90**, 2242–2260 (2023).
26. Haskell, M. W., Nielsen, J. F. & Noll, D. C. Off-resonance artifact correction for MRI: a review. *NMR Biomed.* **36**, 1–24 (2023).
27. Boberg, M., Knopp, T. & Möddel, M. Reducing displacement artifacts by warping system matrices in efficient joint multi-patch magnetic particle imaging. *Int. J. Mag. Part. Imag.* **6**, 2009030 (2020).
28. Albers, H., Knopp, T., Möddel, M., Boberg, M. & Kluth, T. Modeling the magnetization dynamics for large ensembles of immobilized magnetic nanoparticles in multi-dimensional magnetic particle imaging. *J. Magn. Magn. Mater.* **543**, 168534 (2022).
29. Thieben, F. et al. On the receive path calibration of magnetic particle imaging systems. *IEEE Trans. Instrum. Meas.* **72**, 1–15 (2023).
30. O'donnell, M., Karr, S. G., Barber, W. D., Wang, J. M. & Edelstein, W. A. Method for homogenizing a static magnetic field over an arbitrary volume. https://patents.google.com/patent/US4680551A. US Patent US4680551A (1987).
31. Bringout, G. & Buzug, T. A robust and compact representation for magnetic fields in magnetic particle imaging. *Biomed. Tech.* **59**, 978–1 (2014).
32. Boberg, M., Knopp, T. & Möddel, M. Unique compact representation of magnetic fields using truncated solid harmonic expansions. *Eur. J. Appl. Math*. 1–28 (2025).
33. Rinaldi, D. Lamé's functions and ellipsoidal harmonics for use in chemical physics. *Comput. Chem.* **6**, 155–160 (1982).
34. Miloh, T. Maneuvering hydrodynamics of ellipsoidal forms. *J. Ship Res.* **23**, 66–75 (1979).
35. Garmier, R. & Barriot, J.-P. Ellipsoidal harmonic expansions of the gravitational potential: theory and application. *Celest. Mech. Dyn. Astron.* **79**, 235–275 (2001).
36. Svarnas, P. et al. Influence of atmospheric pressure guided streamers (plasma bullets) on the working gas pattern in air. *IEEE Trans. Plasma Sci.* **42**, 2430–2431 (2014).
37. Crozier, S., Forbes, L. K. & Brideson, M. Ellipsoidal harmonic (Lamé) MRI shims. *IEEE Trans. Appl. Supercond.* **12**, 1880–1885 (2002).
38. Punzo, V., Besio, S., Pittaluga, S. & Trequattrini, A. Solution of Laplace equation on non axially symmetrical volumes. *IEEE Trans. Appl. Supercond.* **16**, 1815–1818 (2006).
39. Besio, S., Pittaluga, S., Punzo, V. & Trequattrini, A. Elliptical coils for dedicated MRI magnets. *IEEE Trans. Appl. Supercond.* **18**, 908–911 (2008).
40. Pittaluga, S., Besio, S., Punzo, V. & Trequattrini, A. Racetrack coils for dedicated MRI magnets. *IEEE Trans. Appl. Supercond.* **20**, 786–789 (2010).
41. Dassios, G. & Sleeman, B. D. A note on the reconstruction of ellipsoids from the x-ray transform. *Math. Med. Biol.: A J. IMA* **8**, 141–147 (1991).
42. Dassios, G. *Electric and Magnetic Activity of the Brain in Spherical and Ellipsoidal Geometry*, 133–202 (Springer Berlin Heidelberg, Berlin, Heidelberg, 2009).
43. Law, S., Nunez, P. & Wijesinghe, R. High-resolution eeg using spline generated surface laplacians on spherical and ellipsoidal surfaces. *IEEE Trans. Biomed. Eng.* **40**, 145–153 (1993).
44. Fragoyiannis, G. & Vafeas, P. A semi-analytical approach for the computation of ellipsoidal harmonics. *J. Comput. Appl. Math.* **437**, 115418 (2024).
45. Bardhan, J. P. & Knepley, M. G. Computational science and re-discovery: open-source implementation of ellipsoidal harmonics for problems in potential theory. *Comput. Sci. Discov.* **5**, 014006 (2012).

46. Hobson, E. W. *The Theory of Spherical and Ellipsoidal Harmonics* (Cambridge University Press, 1931).
47. Arnaoudov, I. & Venkov, G. Relations between spheroidal and spherical harmonics. *Dokl. Bolg. Akad. Nauk* **63**, 7 (2010).
48. Gil, A. & Segura, J. A code to evaluate prolate and oblate spheroidal harmonics. *Comput. Phys. Commun.* **108**, 267–278 (1998).
49. Shaqfa, M. & van Rees, W. M. Spheroidal harmonics for generalizing the morphological decomposition of closed parametric surfaces. *Constr. Build. Mater.* **454**, 138967 (2024).
50. Scheffler, K. et al. Ellipsoidal harmonic expansions for efficient approximation of magnetic fields in medical imaging. In *Conference Proceedings Published as Supplement in the International Journal on Magnetic Particle Imaging*, Vol. **10**, 1–4 (2024).
51. O'Reilly, T., Teeuwisse, W. M. & Webb, A. G. Three-dimensional MRI in a homogenous 27 cm diameter bore Halbach array magnet. *J. Magn. Reson.* **307**, 106578 (2019).
52. De Vos, B., Fuchs, P., O'Reilly, T., Webb, A. & Remis, R. Gradient coil design and realization for a halbach-based MRI system. *IEEE Trans. Magn.* **56**, 3 (2020).
53. Dassios, G. *Ellipsoidal Harmonics - Theorie and Applications* (Cambridge University Press, 2012).
54. Foerger, F. et al. Single-shot magnetic field measurements for mpi. In *13th International Workshop on Magnetic Particle Imaging*, 1. https://www.journal.iwmpi.org/index.php/iwmpi/article/view/743 (2024).
55. Beentjes, C. H. L. Quadrature on a spherical surface. Tech. Rep. https://cbeentjes.github.io/files/Ramblings/QuadratureSphere.pdf (2015).
56. Zhou, Y. & Chen, X. Spherical t_ε-designs for approximations on the sphere. *Math. Comput.* **87**, 2831–2855 (2018).
57. Zhou, Y. Quadrature rules with neighborhood of spherical designs on the two-sphere. *Appl. Math. Comput.* **367**, 124769 (2020).
58. Womersley, R. S. *Efficient Spherical Designs with Good Geometric Properties*, 1243–1285 (Springer International Publishing, Cham, 2018).
59. Byerly, W. E. *An Elementary Treatise on Fourier's Series and Spherical, Cylindrical, and Ellipsoidal Harmonics, With Applications to Problems in Mathematical Physics* (Ginn & Company, 1893).
60. Panou, G. A Study on Geodetic Boundary Value Problems. In *Ellipsoidal Geometry*. Ph.D. thesis. National Technical University of Athens (2014).

Acknowledgements

We acknowledge financial support from the Open Access Publication Fund of UKE - Universitätsklinikum Hamburg-Eppendorf.

Author contributions

K.S. contributed to conceptualization and theory, implemented the software, performed the studies and wrote the original draft. L.M. contributed to the theory. F.F. contributed to field simulations and conceptualization. M.B. contributed to conceptualization and comprehensibility of the theory. M.M. contributed to conceptualization and comprehensibility of the theory. T.K. contributed to the conceptualization and supervised the project. All authors reviewed the final manuscript.

Funding

Open Access funding enabled and organized by Projekt DEAL.

Competing interests

The authors declare no competing interests.

Additional information

Correspondence and requests for materials should be addressed to Konrad Scheffler.

Peer review information *Communications Physics* thanks the anonymous reviewers for their contribution to the peer review of this work.